Journal of Molecular Structure 1214 (2020) 128183

Contents lists available at ScienceDirect

Journal of Molecular Structure

journal homepage: http://www.elsevier.com/locate/molstruc

Crystal engineering and electrostatic properties of co-crystals of pyrimethamine with benzoic acid and gallic acid

Muhammad U. Faroque [a], Arshad Mehmood [b], Sajida Noureen [a], Maqsood Ahmed [a, *]

[a] Materials Chemistry Laboratory, Department of Chemistry, The Islamia University of Bahawalpur, 63100, Bahawalpur, Pakistan
[b] Department of Chemistry & Biochemistry, Texas Christian University, Fort Worth, Texas, 76129, USA

ARTICLE INFO

Article history:
Received 8 January 2020
Received in revised form
26 March 2020
Accepted 31 March 2020
Available online 12 April 2020

Keywords:
Pyrimethamine
Gallic acid
Benzoic acid
Co-crystal
Crystal structure
ELMAM2
MoPro

ABSTRACT

Crystal structures of co-crystal salt forms of anti-malarial drug pyrimethamine with benzoic acid in water solvent **(I)** and gallic acid in ethanol solvent **(II)** have been studied using X-ray diffraction data collected at room temperature. Refinement of crystal structures were carried out by independent atomic model (IAM), while the electrostatic properties were studied by transferring electron density parameters from an electron density database. Theoretically optimized hydrogen bond distances were used in the refinement procedures as they were found superior to the neutron diffraction distances. Results of both refinements were compared. Three dimensional Hirshfeld surface analysis and two dimensional fingerprint maps of individual molecules are dominated by H···H and O···H/H···O contacts. Topological analysis was carried out using Bader's theory of Atoms In Molecules (AIM). Electrostatic properties such as dipole moment and electrostatic potential were calculated. Results of this study reveal that the co-crystal formation takes place due to N–H···O/N–H···O homosynthon. Quantitative and qualitative analysis shows that the synthon is robust one. Density functional theory (DFT) based calculations used to elucidate the factors which drive the co-crystallization, complement the experimental findings. The study highlights the significance of using multipolar parameters to understand the phenomena involved in crystal engineering.

1. Introduction

In recent years, crystal engineering has mainly focused on novel compositions of multi-component crystallization with controllable structure and desired physicochemical properties. Co-crystallization is of great importance in broad spectrum of fields such as optoelectronics [1,2] gas storage or separation [3] and pharmaceuticals [4]. Relevance of co-crystallization to pharmaceutical sciences is high due to possibility of rationally designed crystal form of an active pharmaceutical ingredient (API) with biological inactive compound (co-former) that are solids under ambient conditions [5,6]. A co-former may also be another active pharmaceutical ingredient (API) resulting API-API co-crystal. Usually, co-crystal is the new class of compounds possessing combination of the properties of different components with respect to individual components in a crystal lattice. Synthesizing such crystalline material and its applications represent a unique approach in pharmaceutical industry [5]. The current interest is in pharmaceutical co-crystals relevance to the GRAS (Generally Regarded As Safe) co-formers leads to many potential co-crystals improving physicochemical properties of API without affecting its pharmacological activity and breaking or making covalent bonds [6–8]. Clearly the co-former used to synthesize co-crystal should be safe in all aspects.

Path for the development of co-crystals follows a clear step, which is no longer based on fortune, but on rational design of solid forms is a part of crystal engineering [9]. The strategy of crystal engineering to form co-crystal can be attributed to the exterior functional group of API to form supramolecular synthons, especially hydrogen bonding supramolecular synthon with a variety of pharmaceutically acceptable co-formers [10] Design for API with multiple functional groups is challenging [11]. The adopted strategy includes the binding sites present in the co-formers, considering the proposed supramolecular synthons and hydrogen bond reciprocity are major factors [12]. Stoichiometric ratios of different drug

* Corresponding author.
E-mail addresses: Umer.faroque@iub.edu.pk (M.U. Faroque), arshad.mehmood@tcu.edu (A. Mehmood), sajida.noureen@iub.edu.pk (S. Noureen), maqsood.ahmed@iub.edu.pk (M. Ahmed).

https://doi.org/10.1016/j.molstruc.2020.128183
0022-2860/

co-former based on the predicted supramolecular synthons can be explored. Formation of co-crystals is due to non-covalent interactions such as π−π interaction, van der Waals interaction, hydrogen bonding and ionic interactions. Non covalent interactions are of biological importance because bio-molecules are held together by weak interactions. Due to dynamic nature of these biochemical reactions these are responsible for processes occurring in the living organisms [13]. Among non-covalent interactions hydrogen bonding is the most important interaction playing a vital role in material study [14,15]. Supramolecular synthon and hydrogen bond motifs play an important role in crystal engineering [13,16]. The binding mechanism of a molecule to an active site depends upon the charge density distribution, strength of the intermolecular interactions, directionality and the charges on the participating atoms in the intermolecular interactions [17] and this results supramolecular frame work [18]. Co-crystallization reactions can also be followed by charge transfer from one component of the crystal to other component resulting in salt formation [17]. The topology of the intermolecular interactions, understanding the electrostatic properties and knowledge of the physicochemical properties may allow researchers to redesign a drug in order to reduce side effects [19,20]. In order to estimate inter & intramolecular interaction energy, high quality structural data is required. A small change in geometrical parameters of molecule can result into a significant change in the conformational energy. So it is important to note not only which parameter undergo change but also the magnitude of that change. In X-ray diffraction, quality of structural data depends upon several factors such as maximum diffraction angle $\theta_{max}/2\theta_{max}$ should be such that $(\sin\theta/\lambda)_{max}$ 0.6 $Å^{-1}$ ($\theta_{max} \geq 25^{\circ}$ for Mo Kα; $\theta_{max} \geq 67^{\circ}$ for Cu Kα). Electron density model of refinement is another crucial factor which affects the structural parameters. In order to determine electron density distribution in a molecule, multipolar refinement has to be carried out which requires a high resolution (d = 0.5 Å) X-ray diffraction data. But there are certain limitations that not every crystal diffracts to high resolution. Moreover, every laboratory is not equipped with cryo-cooling facility. So, transferability principle [21] is applied to low resolution X-ray diffraction data. Various parameters from an electron-density database can be transferred on the basis of the chemical environment, similarity of atom types to overcome low-resolution data [22]. Several databases have been constructed, such as the UBDB [23], Invariom database [24], ELMAM [25] and its improved version ELMAM2 [26]. Several studies have exploited the aspherical atom databases in routine crystallographic modeling [27−31] and have successfully shown that the application of the method results in a notably improved molecular geometry, superior refinement statistics, a better description of the thermal motion and an improvement of phases.

Furthermore, after successful application of transferability principle we can calculate a number of charge density derived properties such as dipole moment, electrostatic potential and topological analysis of covalent non-covalent interactions with better refinement of structural parameters, i.e. scale factors, atomic coordinates and displacement parameters. After suitable electron density modeling, residual electron density maps are improved and residual electron density peaks localized on covalent bonds disappear.

Pyrimethamine is used for treatment of cystoisosporiasis caused by *Cystoisospora belli*. This drug is preferred as alternative treatment of acute C. belli infections, malaria, pneumonia and toxoplasmosis in HIV affected peoples who fail to tolerate co-trimoxazole drug (NIH, USA, 2013). Resistance to pyrimethamine is widespread. Mutation in malarial gene for dihydrofolate reductase may reduce drug effectiveness [32]. This mutation is responsible for decreasing binding affinity between dihydrofolate reductase and pyrimethamine through steric interactions and loss of H-bonds [33]. Benzoic acid is a common co-former occurs naturally in many plants used as a good precursor in organic synthesis and it's salts can be used as food preservatives. Fungal skin diseases such as ringworm, tinea and athlete's foot can be cured by benzoic acid [34]. Gallic acid is trihydroxybenzoic acid, which occurs naturally in land plants, different oak species, Various foodstuff contains different amount of gallic acid especially fruits including grapes, bananas and strawberry [35−37]. Gallic acid has been implicated as anti-inflammatory agents, anticarcinogenic, antimutagenic, antimicrobial and antiangiogenic agents. Besides these this is also being used in critical diseases like lipid related disease, cancer and depression [38].

In this scientific contribution, by using knowledge based strategy we were able to synthesize co-crystals of pyrimethamine (API) with benzoic acid **I** and pyrimethamine with gallic acid **II** (Scheme 1) using crystal structure prediction methodology. Crystal structure prediction method will be abbreviated as CSP in this text. In this study we reported their characterization by single crystal X-ray diffraction (SCXRD), thermogravimetric analysis (TGA) and computational study for atomic charges as well as energies of both moieties **I** and **II**. Most CSP methods rely on the assumption that observed crystal structure lie within small energy range and are most stable. Cambridge crystallographic data center (CCDC) is a good source for CSP which is the computational method utilized as a test of model for intermolecular interactions in small molecules. The core of this methodology is 'supramolecular synthon'. In CSP exercise the synthons resulted from O−H···N and N−H···O interactions were analyzed [12,39−60]. Following CSP strategy we were able to synthesize our interested API with two different co-formers.

2. Experimental

2.1. Synthesis and crystallization

For synthesis of **I** an equimolar ratio (1:1) of pyrimethamine (API) and benzoic acid (co-former) in methanol were refluxed for 2 h. Single crystals were obtained after one week, by slow evaporation of solvent at room temperature.

The same method is applied to co-crystallize pyrimethamine and gallic acid for **II**. Instead of methanol, ethanol was used as a solvent. Single crystals appeared after few days by slow evaporation at room temperature.

2.2. Single crystal X-ray diffraction; structure solution and refinement

Single crystal diffraction measurements for both co-crystals **I** and **II** were performed at room temperature on a Bruker D8 venture Single Crystal X-rays diffractometer with PHOTON II detector. The experiment for **I** was carried out using Cu *Kα* radiations (λ = 1.5406 Å) and for **II** was carried out Mo *Kα* radiations (λ = 0.71073 Å). The structures were solved using Olex 2 [61] program and refined against F^2 by weighted full matrix least square method using SHELX(62). The crystallographic data for the structures have been deposited in Cambridge crystallographic data center with CCDC Deposition Number 1975120−1975,122 for **I** and 1,975,145−1975,147 for **II**. ORTEP-3 for Windows [63] and Mercury [64] software were used to prepare material for publication. Fig. 1 shows the thermal ellipsoid diagrams along with atom numbering scheme for non-hydrogen atoms.

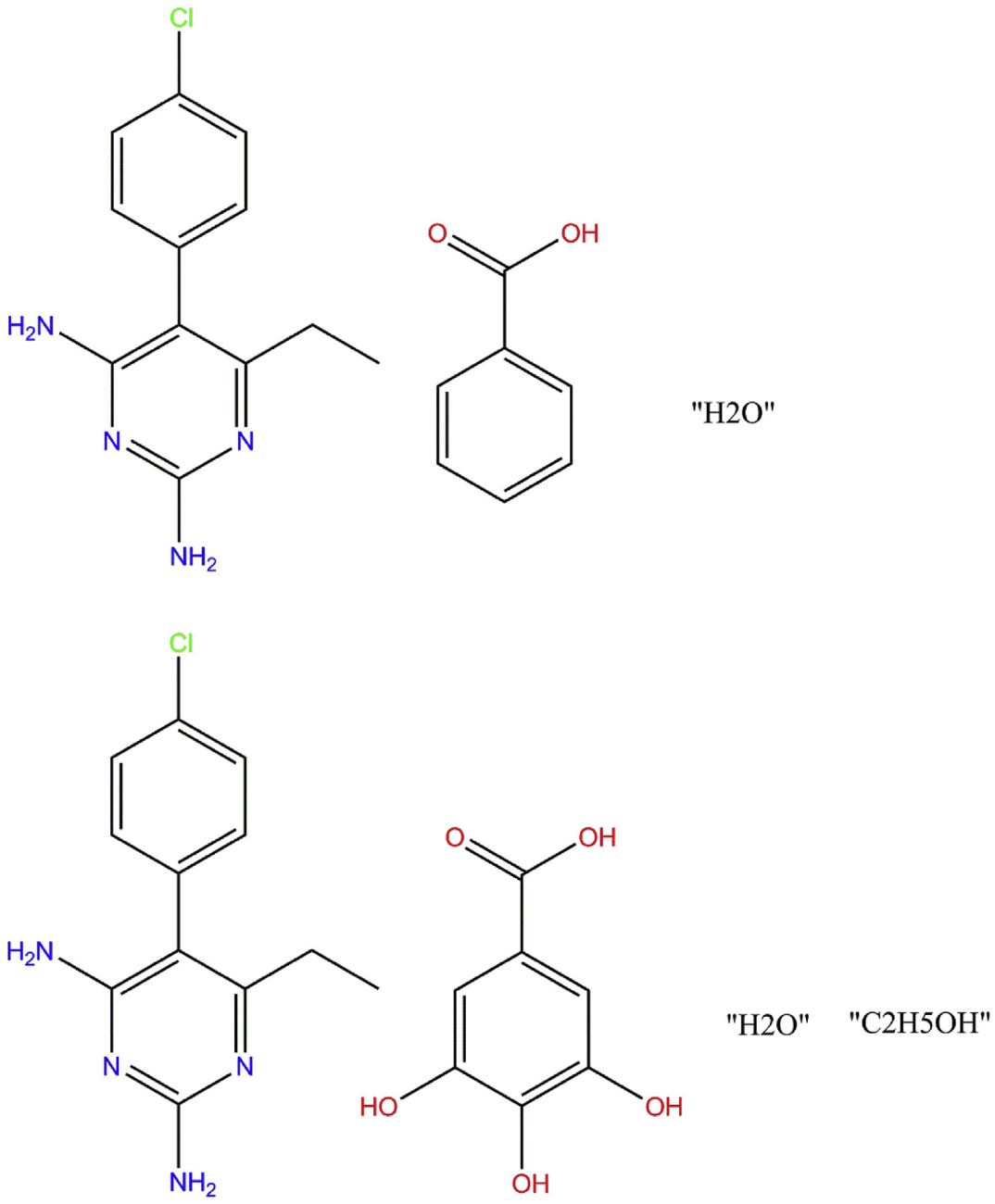

Scheme 1.

2.3. MoPro IAM refinement

The model of **I** and **II** was subsequently imported to MoPro software [65], C–H bond lengths were constrained to standard neutron values [66]. However, the optimized C–H distances obtained from theoretical values (details mentioned below in section 2.5) calculated from density functional theory (DFT) were found to ameliorate the statistics, hence were used in the subsequent refinements. H atoms attached to heteroatoms were refined freely in compound **I** and had to be restrained in compound **II** with a su of 0.001. A full matrix least square refinement of IAM (Independent atomic model) was performed according to the all intensity data. SHELX weighting scheme was adopted with a = 0.12950, b = 0.63480 for **I** and a = 0.06340, b = 1.23600 for **II** [2,61]. Subsequently, displacement parameters of non H atoms were refined. The anisotropic displacement parameters for the H atoms were constrained to calculated values from the SHADE server [67]. Here and in our previous study [68] we have demonstrated that anharmonic refinement for Cl atom in Pyrimethamine moiety improves results despite ordinary resolution and ambient data conditions [69]. In this conventional (IAM) model refinement atomic positions, scale factors and displacement parameters for all atoms were refined using MoPro program [65,70] until convergence.

In compound **I**, at the end of IAM refinements, crystallographic *R* factor *R* [$F^2 > 2\sigma(F^2)$] was 0.060, the weighted *R* factor w*R* (F^2) was 0.197 and goodness of fit 0.83. The minimum and maximum electron density peaks were −0.23 and 0.28 e/Å^{-3}respectively.

In compound **II**, at the end of IAM refinements, crystallographic R factor *R* [$F^2 > 2\sigma(F^2)$] was 0.097, the weighted *R* factor w*R* (F^2) 0.092 and goodness of fit 1.23. The minimum and maximum

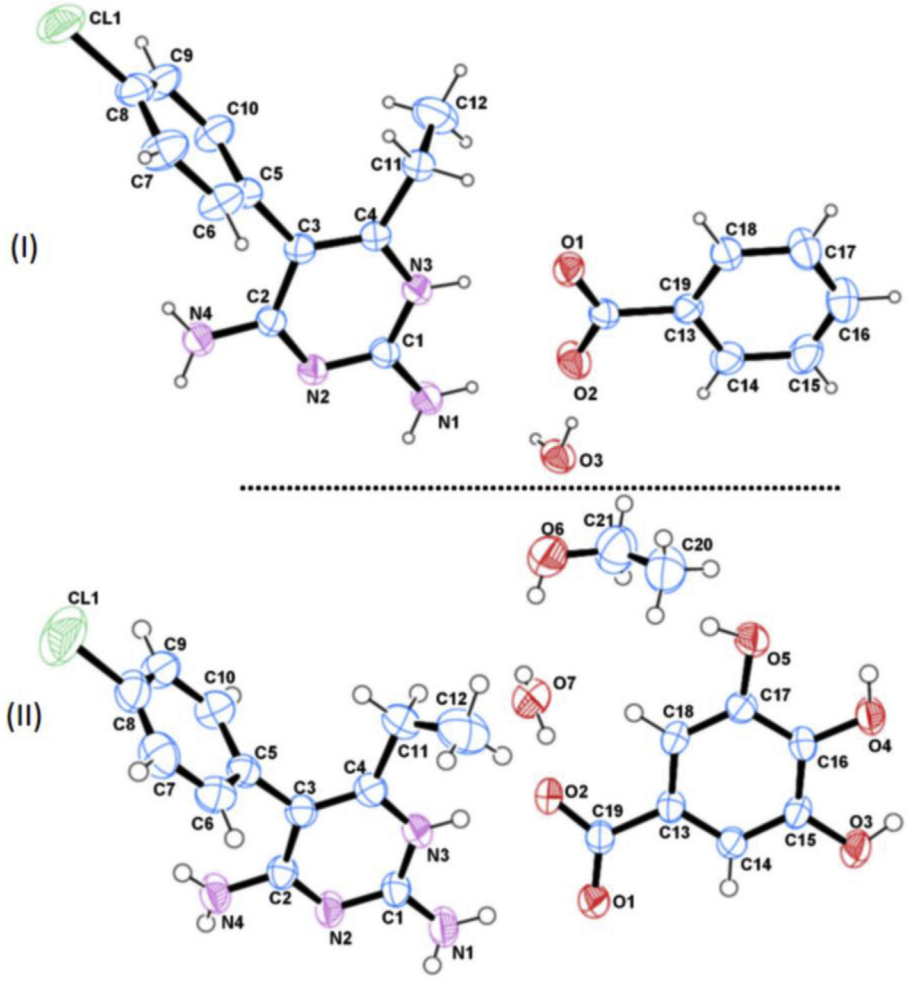

Fig. 1. A displacement ellipsoid diagram based on ELMAM2 model drawn at 50% probability level showing atoms numbering scheme.

electron density peaks were −0.49 and 0.56 e/Å^{-3}respectively.

2.4. MoPro ELMAM2 refinement

In the ELMAM2 [25,71] refinements for both **I** and **II**, same parameters were varied as in IAM refinement except multipolar charged atomic model was applied and refined till convergence. The electron density parameters were transferred from ELMAM2 library and kept fixed. The model was electrically neutralized at the end. ELMAM2 refinement had a noticeably improved refinement statistics; In compound **I**, at the end of ELMAM2 refinements, the crystallographic *R* factor *R* [$F^2 > 2\sigma(F^2)$] was 0.059, the weighted *R* factor w*R* (F^2) 0.200 and goodness of fit *S* 0.85. The minimum and maximum electron density peaks were −0.25 and 0.38 e Å^{-3}, respectively. In compound **II**, the crystallographic *R* factor *R* [$F^2 > 2\sigma(F^2)$] was further reduced from 0.097 to 0.093, the weighted *R* factor w*R* (F^2) 0.091 to 0.088 and goodness of fit *S* 1.23 to 1.19. The minimum and maximum electron density peaks were −0.48 and 0.58 e Å^{-3}respectively. Crystal data, data collection and refinement statistics details of I and II are summarized in the Tables 1 and 2 respectively.

2.5. Computational details

The density functional theory (DFT) based theoretical calculations on **I** and **II** were performed in two stages. A preliminary partial geometry optimization was carried out using periodic DFT-D3 method starting with the lattice parameters and atomic positions obtained from the standard neutron distances based Mopro IAM refinements. All non-hydrogen atoms in the unit cell were fixed and only hydrogen atoms were allowed to relax during the optimization using the Quantum-Espresso [72] (QE) suite of programs. Ultra-soft pseudopotentials were used for all atoms using the Perdew–Burke–Ernzerh (PBE) [73] exchange–correlation approximation in combination with Grimme's D3 correction for dispersion interactions [74]. The hydrogen atoms were relaxed until the forces exerted on the atoms were less than 10^{-4} (a.u) with 10^{-7} (a.u) convergence threshold on total energy. The cutoff energy and electronic density of plane-waves was set to be 60 Ry and 550 Ry respectively for **I** and 55 Ry and 625 Ry respectively for **II**. The mesh of the unit cell for k-point sampling was 3 × 2 × 3 which corresponds to ~0.2/Å of k-space resolution. The obtained hydrogen distances were used for further Mopro IAM and ELMAM2 refinements.

In the second stage, two types of calculations were carried out using the coordinates obtained after optimized hydrogen distances based ELMAM2 refinements. A periodic DFT-D3 single point energy calculation was performed using all-electron frozen-core PAW [75] methodology on a dense real-space grid comprising of 180 × 432 × 360 points along the crystallographic axes. PBE exchange–correlation approximation was used with enhanced k-point sampling of 6 × 4 × 4 which corresponds to the resolution of

Table 1
Crystal data and data collection statistics.

Crystal data	Compound I	Compound II
Chemical Formula	$C_{19}H_{21}ClN_4O_3$	$C_{21}H_{27}ClN_4O_7$
Mr	388.83	482.91
Crystal system	Monoclinic	Monoclinic
Space group	$P2_1/c$	$P2_1/c$
Temperature (K)	239	296
a,*b*,*c* (Å)	9.7703 (2), 15.1624 (3), 13.7502 (3)	9.4025 (14), 18.956 (3), 12.7918 (17)
B(°)	93.9670	90.724 (5)
V (Å^3)	2032.09 (7)	2279.8 (6)
Z	4	4
Radiation type	Cu, λ = 1.54178 Å	Mo *Kα*, λ = 0.7107 Å
μ (mm^{-1})	1.88	0.22
Crystal size (mm)	0.11 × 0.1 × 0.06	0.53 × 0.31 × 0.15
Data collection		
T_{min}, T_{max}	0.205, 0.355	0.205, 0.355
Measured reflections	41,631	29,698
Independent reflections	3819	4644
Observed reflections	2533 [> 2.0σ(*I*)]	3269 [*I* > 2σ(*I*)]
R_{int}	0.070	0.078
(Sin θ/λ)$_{max}$ (Å^{-1})	0.610	0.610

Table 2
Refinement statistics.

Refinement	SHELX (I)	MoPro (IAM) (I)	MoPro (ELMAM) (I)
R [F^2 > 2σ(F^2)], w*R* (F^2), *S*	0.071, 0.252, 1.68	0.060, 0.197, 0.83	0.059, 0.200, 0.85
No. of reflections	3831	3819	3819
No. of parameters	248	317	433
No. of restraints	0	21	0
H-atom treatment	H-atom parameters constrained	Only H-atom coordinates refined	Only H-atom parameters refined
(Δ/σ)$_{max}$	0.001	0.128	0.001
Refinement	**SHELX (II)**	**MoPro (IAM) (II)**	**MoPro (ELMAM) (II)**
R [F^2 > 2σ(F^2)], w*R* (F^2), *S*	0.054, 0.149, 1.04	0.058, 0.149, 0.99	0.054, 0.141, 0.95
No. of reflections	4644	4597	4596
No. of parameters	336	389	389
No. of restraints	0	27	27
H-atom treatment	H atoms treated by a mixture of independent and constrained refinement	Only H-atom coordinates refined	Only H-atom coordinates refined
(Δ/σ)$_{max}$	<0.001	0.148	−0.128

~0.1/Å. The obtained electron density was used to calculate the Bader charges using Bader analysis program of Henkelman et al. [76]. A gas phase geometry optimization of **I** and **II** was carried out using Gaussian 09 [77] suits of program at M062X [78]/6-31 g(d) level. The corrections for basis set superposition error and dispersion interactions were invoked by using Boys-Bernardi counterpoise method [79] and Grimme's D3 methods respectively as implemented in Gaussian 09. Improved electronic energies were obtained from single-point calculations at M062X/6−311++g (2d, 2p) level for the calculations of Bader charges, vibrational frequencies and other properties using Multiwfn program [80].

3. Results and discussion

3.1. Residual maps and structure description

3.1.1. Compound I

Superiority of transferred model (ELMAM2) over spherical independent atomic model (IAM) has been illustrated in the form of residual maps (Fig. S1) in supplementary information. In these maps (Fig. S1) un-modelled electron density peaks are concentrated on the bonds in IAM whereas these peaks are diminished significantly in ELMAM2. One pyrimethaminium cation, one benzoate anion and a water molecule is present in asymmetric unit cell of co-crystal assembly (Fig. 2).

In our previous study, crystal engineering of API pyrimethamine in our lab results that co-crystal assembly exists as a charge transfer salt [68] and co-crystallization proton transferred salt has been studied in different literature [17]. This co-crystal assembly is also stabilized as a charge transfer salt in which an acidic proton from benzoic acid molecule in the asymmetric unit has been transferred to more basic nitrogen N3 in pyrimethamine. The torsion angle C2−C3−C5−C10 measured between pyrimidine ring and 4-chlorobenzene is −99.65 (3)^0 and the dihedral angle calculated between planes of 4-chlorobenzene and pyrimidine ring is 79.84 (3)^0. Thus pyrimidine is not co-planar with 4-chlorobenzene. Pyrimidine ring in pyrimethamine acts as a donor interacts with acceptor benzoate anion via N1−H1B···O2 and N3−H3···O1 to form a supramolecular synthon "G1" with graph set notation R^2_2 (8). Supramolecular synthon is in planar position with a deviation of 0.262 Å distance from benzene ring in benzoic acid. Water molecule has a key role in this co-crystal assembly; it acts as donor and an acceptor in the formation of hydrogen bond. Water molecule acting as a hydrogen bond donor species forms contacts via O3−H3B···O1^{ii} and O3−H3A···O2 whereas also acting as hydrogen bond acceptor species it forms N4−H4A···O3^{iii} contact. Hydrogen bond with their symmetry codes are given in Table 3.

3.1.2. Compound II

One pyrimethaminuim cation, one 3,4,5-trihydroxybenzoic acid commonly known as gallic acid, one ethanol molecule and one water molecule is present in asymmetric unit cell of co-crystal

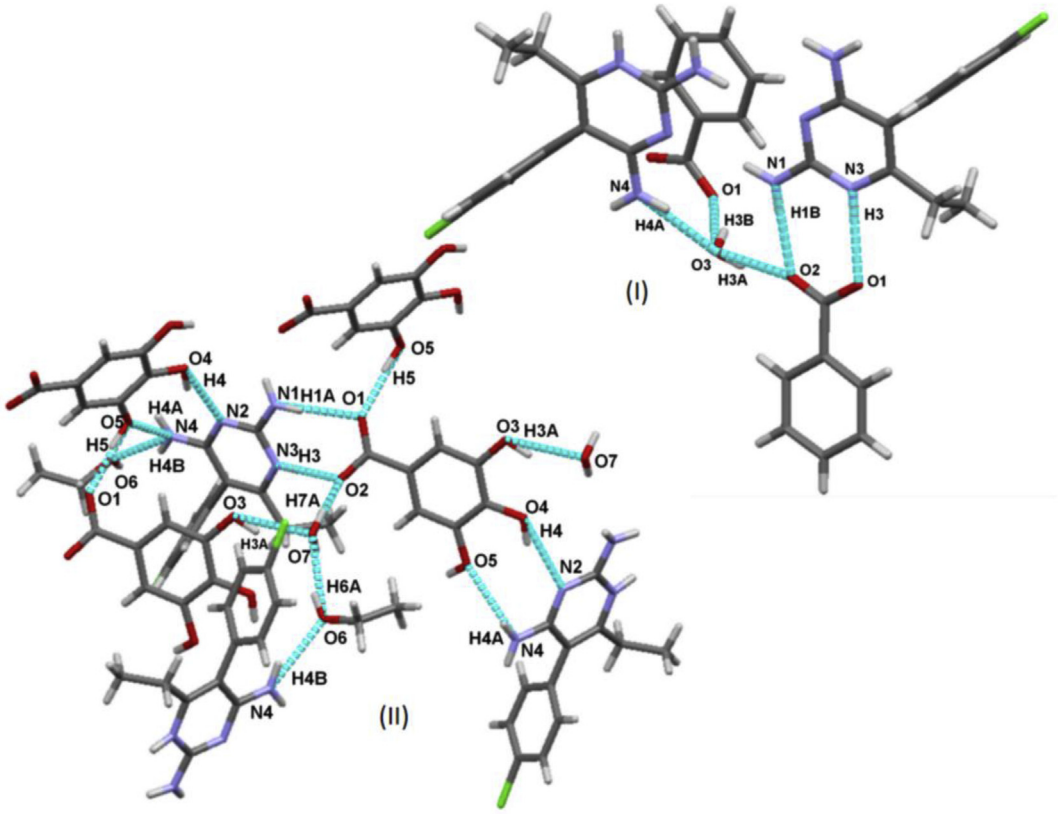

Fig. 2. A view of intermolecular interactions of both **I** and **II** showing rings and synthons.

Table 3
Hydrogen bond geometry of (I).

D—H···A (Å)	D—H(Å)	H···A(Å)	D···A(Å)	D—H···A(Å)
O3—H3A···O2	1.00 (7)	1.71 (8)	2.666 (4)	159.(2)
N3—H3···O1	1.07 (4)	1.66 (5)	2.716 (3)	166.(1)
N3—H3···O2	1.07 (4)	2.61 (4)	3.461 (4)	135.(2)
N3—H3···C19	1.07 (4)	2.43 (4)	3.468 (4)	163.(1)
N1—H1B···O2	1.08 (4)	1.72 (4)	2.796 (4)	175.4 (6)
N1—H1B···C19	1.08 (4)	2.60 (4)	3.582 (4)	152.(2)
N4—H4B···C5	1.11 (5)	2.40 (6)	2.823 (4)	100.(3)
N4—H4B···C6	1.11 (5)	2.53 (6)	3.229 (5)	120.(3)
C11—H12C···C5	0.94 (18)	2.68 (11)	3.049 (5)	104.(8)
C15—H15···O3^{i}	1.17 (5)	2.43 (5)	3.488 (5)	149.(3)
O3—H3B···O1^{ii}	1.01 (6)	1.93 (9)	2.792 (4)	142.(5)
N1—H1A···N2^{iii}	1.10 (4)	2.15 (4)	3.236 (4)	169.7 (9)
N4—H4A···O3^{iii}	1.07 (6)	1.73 (6)	2.760 (4)	161.(2)
C7—H7···N4^{iv}	0.98 (7)	2.49 (6)	3.445 (5)	165.(2)
C18—H18···Cl01^{v}	1.11 (4)	2.79 (4)	3.568 (4)	127.(2)

Symmetry codes: (i) −x, −y, −z+1; (ii) x, −y+1/2, z−1/2; (iii) −x, −y+1, −z+1; (iv) x, −y+3/2, z+1/2; (v) −x+1, −y+1, −z+2.

assembly (Fig. 2). Pyrimethaminium cation acts as donor species interact with 3,4,5-trihydroxybenzoate anion acceptor via contacts N1—H1A···O1 and N3—H3···O2 to form a supramolecular synthon "M1" with graph set notation R^2_2 (8). 3,4,5-trihydroxybenzoate anion acting as donor species forms a contact O4—H4···N2^{vii} with pyrimethaminium cation and pyrimethaminium cation acting as donor species forms a contact N4—H4A···O5 with 3,4,5-trihydroxybenzoate anion, as a result of these two interactions another supramolecular synthon "M2" appears with graph set notation R^2_2 (8). N4—H4B···O6^{iii} is another interaction of hydrogen bond formed between pyrimethaminium cation (donor) and ethanol (acceptor) molecule. 3, 4, 5-trihydroxybenzoate anion interact with other 3,4,5-trihydroxybenzoate anion via O5—H5···O^{iv} hydrogen bond. Water molecule being an acceptor one interacts with 3, 4, 5-trihydroxybenzoate anion to form O3—H3A···O7^{vi} interaction. Water molecule also forms an interaction O6—H6A···O7 with an ethanol molecule. Hydrogen bonds with their symmetry code are given in Table 4.

Table 4
Hydrogrn bond geometry of (II).

D—H···A	D—H	H···A	D···A	D—H···A
N4—H4B···C6	0.863	2.78	3.3245	122.46
C10—H10···C13^{i}	0.924	2.768	3.591	148.85
O7—H7A···C19	0.849	2.754	3.5728	162.54
N3—H3···C19	0.862	2.719	3.5291	157
N1—H1A···C19	0.867	2.717	3.5385	158.71
C10—H10···C18^{i}	0.924	2.664	3.4967	150.29
C11—H11A···C5	0.976	2.588	3.043	108.55
O7—H7B···O6	0.844	2.514	2.8486	104.73
N1—H1B···O6^{v}	0.811	2.477	3.2218	153.27
N4—H4B···C5	0.863	2.467	2.8304	106.09
N4—H4A···O5^{ii}	0.814	2.433	2.9492	122.23
O4—H4···O5	0.892	2.277	2.7199	110.39
O3—H3A···O4	0.877	2.263	2.7335	113.52
N4—H4B···O6^{iii}	0.863	2.149	2.9038	145.78
N1—H1A···O1	0.867	2.108	2.9686	171.67
O4—H4···N2^{vii}	0.892	2.086	2.9064	152.45
O6—H6A···O7	0.82	2.066	2.8486	159.43
O3—H3A···O7^{vi}	0.877	2.03	2.8111	147.78
O7—H7A···O2	0.849	1.977	2.7035	142.94
N3—H3···O2	0.862	1.794	2.6556	178.24
O5—H5···O1^{iv}	0.941	1.746	2.6814	172.71

Symmetry codes: (i) −x, −y, −z+1; (ii) x, −y+1/2, z−1/2; (iii) −x, −y+1, −z+1; (iv) x, −y+3/2, z+1/2; (v) −x+1, −y+1, −z+2.

3.2. Hirshfeld surface analysis and fingerprint plots

Hirshfeld surface and fingerprint plots were generated for both co-crystals **I** & **II** by using Crystal Explorer [81,82]. Intermolecular interactions can be visualized by Hirshfeld surface with different colors and colors intensity, indicating short and long contacts and strength of these contacts (Fig. 3). These were mapped over d_{norm} based on van der Waal's radii mapped onto Hirshfeld surface, where the red circular depressions are visible in the surface indicating strong hydrogen bonding contacts. Blue area in the Hirshfeld surface is representing the d_{norm} value positive which is indicative of a longer distance than the sum of van der Waal's radii. Those intermolecular distances which are close to van der Waal's radii have d_{norm} value zero. Negative d_{norm} values are indicated in red, denoting a shorter distance than the sum of the van der Waal's radii. The shortest and strongest contacts are due to O—H···O [O3—H3B···O1, O3—H3A···O2 for **I** and O5—H5···O1, O3—H3A···O7, O6—H6A···O7 for **II**] and N—H···O [N1—H1B···O2, N3—H3···O1 and N4—H4A···O3 for **I** and N1—H1A···O1, N3—H3···O2, O4—H4···N2, N4—H4A···O5, N4—H4B···O6 for **II**] hydrogen bonds declare certain bright red spots. C—H···O contacts are also visible in the surface as light red spots. So, color intensity demonstrates the intensity of interactions. The bluish area illustrates areas for neighboring atoms are too for apart for there to be interaction between them.

Fig. 4(a)-(b) illustrates the Hirshfeld surface fingerprint plots and percentage contribution of intermolecular interactions of both co-crystals **I** & **II** respectively. Fingerprint plots exhibited in these figures includes reciprocal contacts. Individual FPs of individual molecules incorporated in the crystals was analyzed. In this analysis, the division of contribution of different molecules in a single crystal is possible for different interactions, including O···H, H···H, N···H, C···H and other contacts commonly overlap in full FPs.

3.2.1. Compound I

FPs in Fig. 4(a) labeled **(a)** shows the fingerprints of benzoate anion in which H···H interaction (38.1% area) has the greatest participation in the crystal structure with respect to other contacts. O···H interaction (27.0% area) has the second greatest participation with the most visible pair of sharp spikes which is specific characteristic of O···H interaction. Intermolecular interactions of C···H, CL···H interactions (17.3%, 7.6% area respectively) also has a dominant participation. N···H interaction (3.2% area) has the least contribution in the crystal structure. **(b)** Shows the FPs of pyrimethaminium cation in which H···H interaction (45.3%) has the greatest participation than other contacts. A broad spike illustration is the characteristic of H···H interaction. Fingerprint maps of C···H contacts (17.0% area) appear as symmetrical wings in total Hirshfeld surface. 11.5% area contribution of Cl···H interaction is also present in total Hirshfeld surface. One sharp spike for O···H interaction (9.8% area) is although a small contribution to total Hirshfeld surface (100% area) but this is a strong interaction exhibiting a single sharp spike. N···H contacts include only 7.5% of Hirshfeld surface and a strong interaction shown by two parallel sharp spikes having less than van der waal's distance. Other Cl···C, C···N and C···C contacts (2.3%, 1.9%, and 1.8% respectively) have minor contribution to total Hirshfeld surface. **(c)** Illustrates the FPs of water molecule which has a dominant role in co-crystal assembly possessing O···H, H···H contacts interaction whose contributions are 50.3% and 49.3% respectively.

3.2.2. Compound II

In Fig. 4(b) labeled **(a)** shows the fingerprint plots of pyrimethaminium cation, the major contribution of 38.7% to total Hirshfeld surface is due to H···H contacts, which represents van der Waal's interaction, followed by C···H interactions which contributes 17.6%. C···H interactions contribution is observed as symmetrical wings. While a sharp spike for O···H interactions with 17.1% contribution is observed as strong contact. H···Cl and N···H interactions also participate with 11.2% and 9.6% contributions to total surface; sharp peak visualization with smaller distances is the characteristics of strong interactions. **(b)** Shows the FPs of 3,4,5-trihydroxybenzoate anion with 45.1% area contact contribution of O···H interaction visualized by two sharp spikes concluding the strong interactions. H···H interaction and C···H interactions have a significant role in total surface contribution with 27.5% and 18.9% contribution. N···H and C···C (3.4% and 1.7% respectively) have minor surface contribution. **(c)** Shows the FPs of ethanol molecule, a clear broad peak (characteristics of H···H) of H···H interaction is the greatest surface contribution (53.2% area) to total Hirshfeld surface. The second greatest surface contribution (23.5% area) is of O···H interaction with two sharp spikes. C···H and H···Cl contacts contributions are 14.7% and 5.0% respectively. **(d)** illustrates the FPs

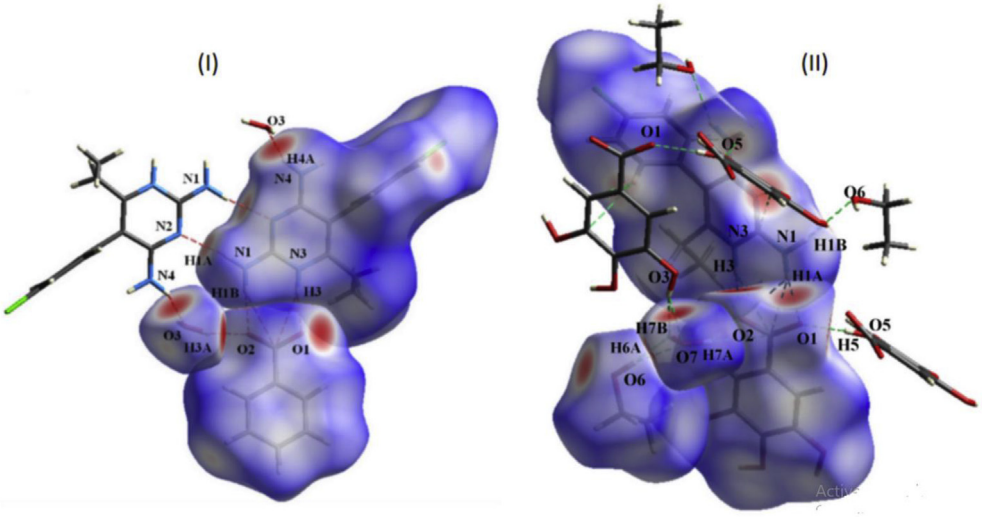

Fig. 3. A Hirshfeld surface based on d_{norm}-property. Red and blue colors represent the distances shorter and longer than the sum of vdW radii and white color represents the distances in between.

of water molecule, in which H···H and O···H interactions have major contribution (48.6%, 42.9%) of interactions, whereas H···Cl and Cl···H also have minor contributions (4.8 and 3.6% respectively).

3.3. Topology of intermolecular interaction

Topology of intermolecular interaction was carried out based on Bader's theory of atoms in molecules (AIM) [65,83] software. In co-crystal assembly **I**, the critical points search in H-bonds gave (3,-1) critical points for non-covalent interactions. N4—H4A···O3 has a short inter atomic distance 1.7256 (5)Å with electron density value 0.268e/Å^{-3} is a noticeable hydrogen bond among all other H bonds in this co-crystal assembly indicates that this character is close to covalent [84]. Moreover the sum of the local energy densities (Gcp + Vcp) value for this interaction is negative which according to Cremer and Kraka (1984) meets the criteria to be partially covalent interaction. O3—H3B···O1 also meet the same criteria and are partially covalent [85]. Whereas, in co-crystal assembly **II** O5—H5···O1 hydrogen bond contact is marked very short inter atomic distance 1.745 Å and value of electron density 0.303e/Å^{-3} is comparable strong hydrogen bond. Hydrogen bond interaction O4—H4···N2 is relatively weak interaction than mentioned above. Inter atomic distance of O4—H4···N2 and O3—H3A···O7 hydrogen bond interactions are 2.087 Å and 2.032 Å respectively with electron density values 0.173e/Å^{-3} and 0.163e/Å^{-3}. The corresponding topological properties and total interaction energies of intermolecular interaction has been calculated. The presence of these interactions justifies the co-crystallization between two moieties. The interaction involving the chlorine atom is weak interaction as it involves C atom as donor species. Both Tables (S1 and S2) of local electron densities of **I** and **II** are given in supplementary information.

3.4. Electrostatic potential and dipole moment

Electrostatic potential is a good tool which provides information about ability of the molecule to bind with neighboring molecules as well as binding of ligands in active sites of enzymes [86—93]. This is a big advantage of the transferability principle that molecular electrostatic potential can be precisely estimated. Coloring the 3D electron density surface according to the electrostatic potential is a useful method to visualize the distribution of charges in the individual moieties or the asymmetric unit. Depending on their affinities molecules in co-crystal arrange themselves in a specific manner. After this arrangement in co-crystal; electrostatic potential of individual molecules vary rather than their pure crystalline form. The electrostatic potential generated by isolated molecules of co-crystal assemblies of **I** and **II** are displayed in Fig. 5.

3.4.1. Compound I

In **I** the negative electrostatic potential (nucleophilic part) is generated not only by the most negatively charged O atoms, O1, O2 and O3, but also by the delocalized electrons of the phenolic ring of benzoate anion. On one side of the co-crystal moiety in pyrimethamine molecule, from H atoms attached to amine group to the methyl group, a large region of positive electrostatic potential electrophilic region is displayed. It is predicted that nucleophilic attack can occur on pyrimethaminium cation electrophilic region.

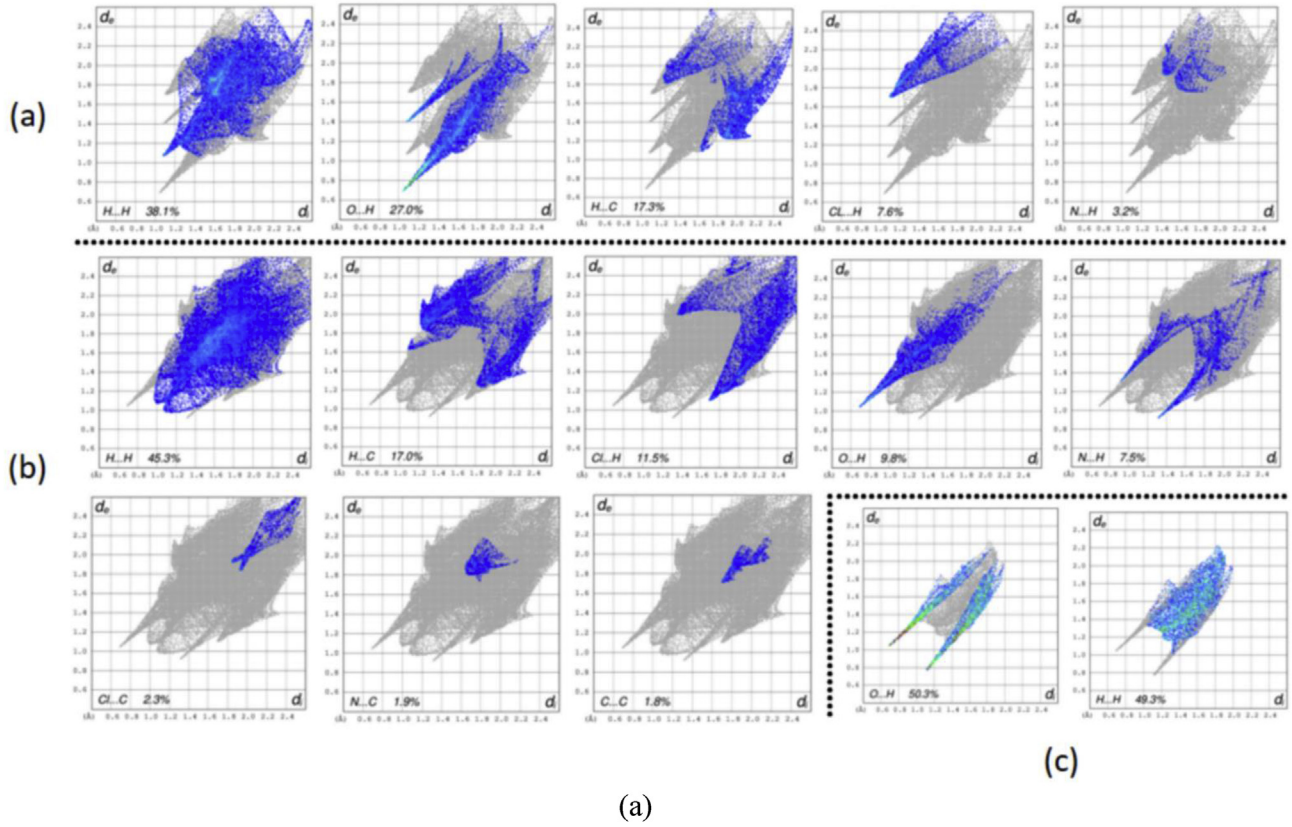

Fig. 4. (a)Fingerprint plots of **I** showing percentage contribution of interactions. (b) Fingerprint plots of **II** showing percentage contribution of interactions.

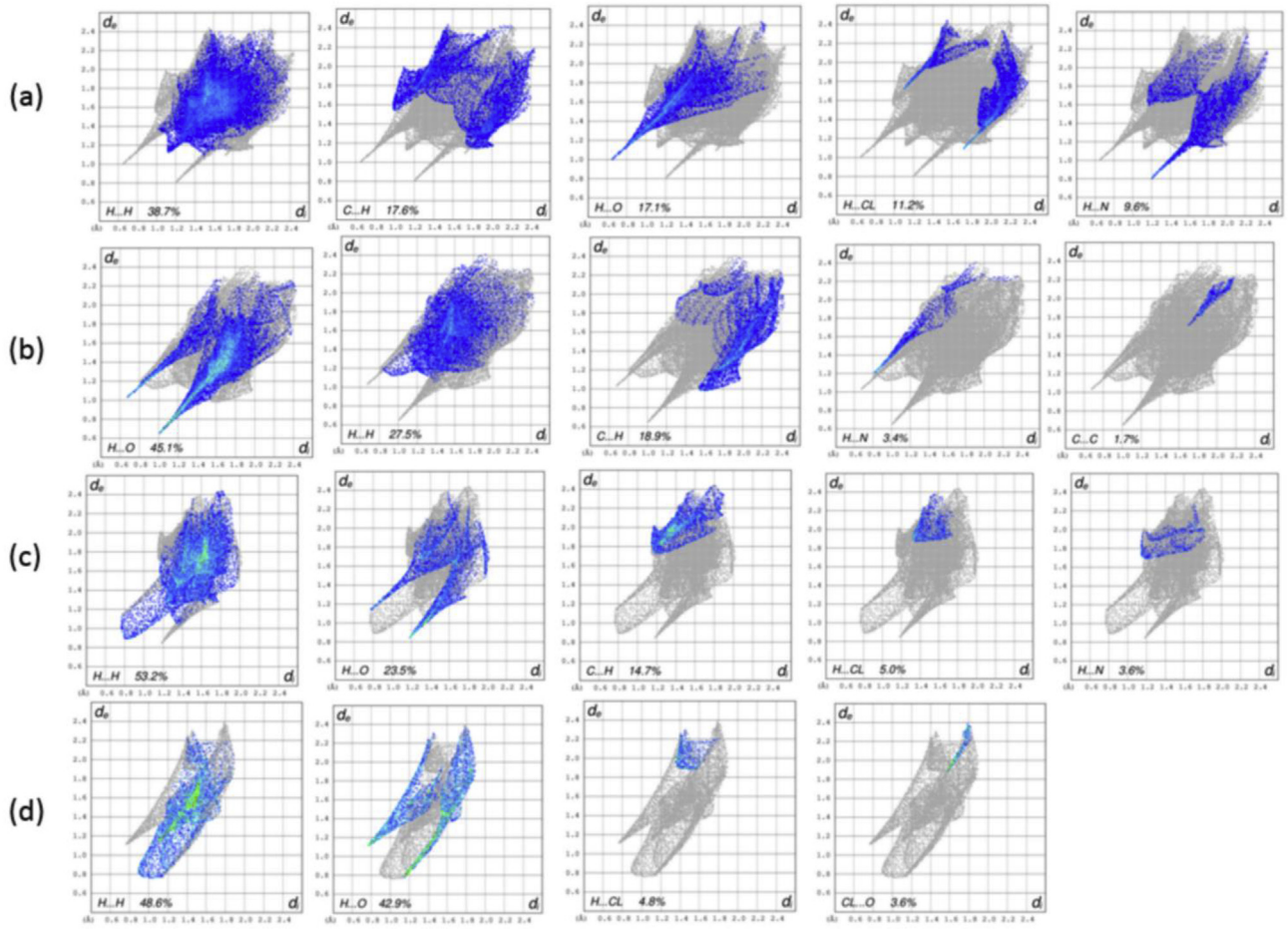

(b)

Fig. 4. (*continued*).

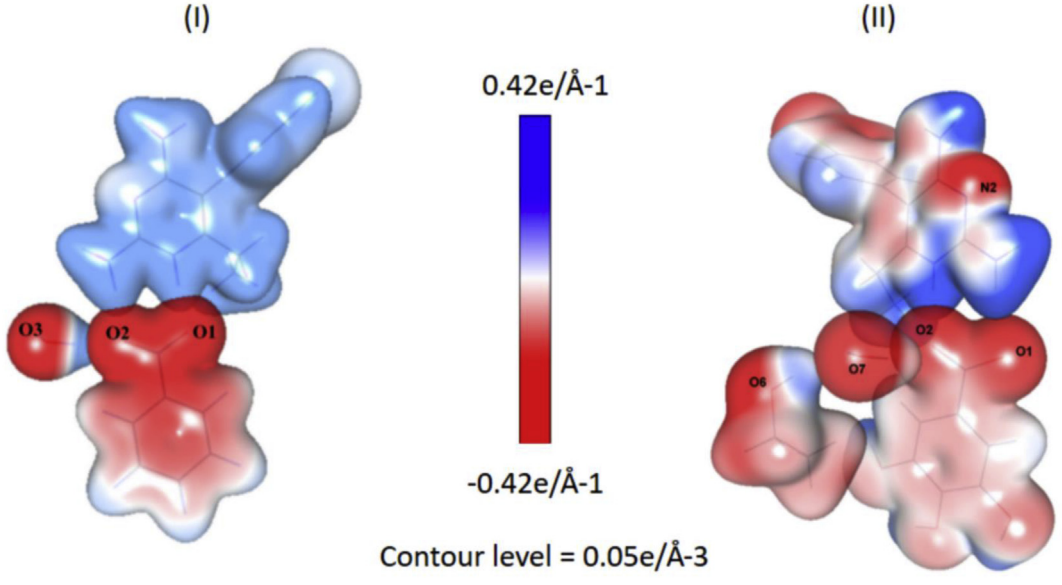

Fig. 5. A 3-D electron density surface colored according to electrostatic potential, separately calculated for each molecule in co-crystal assembly.

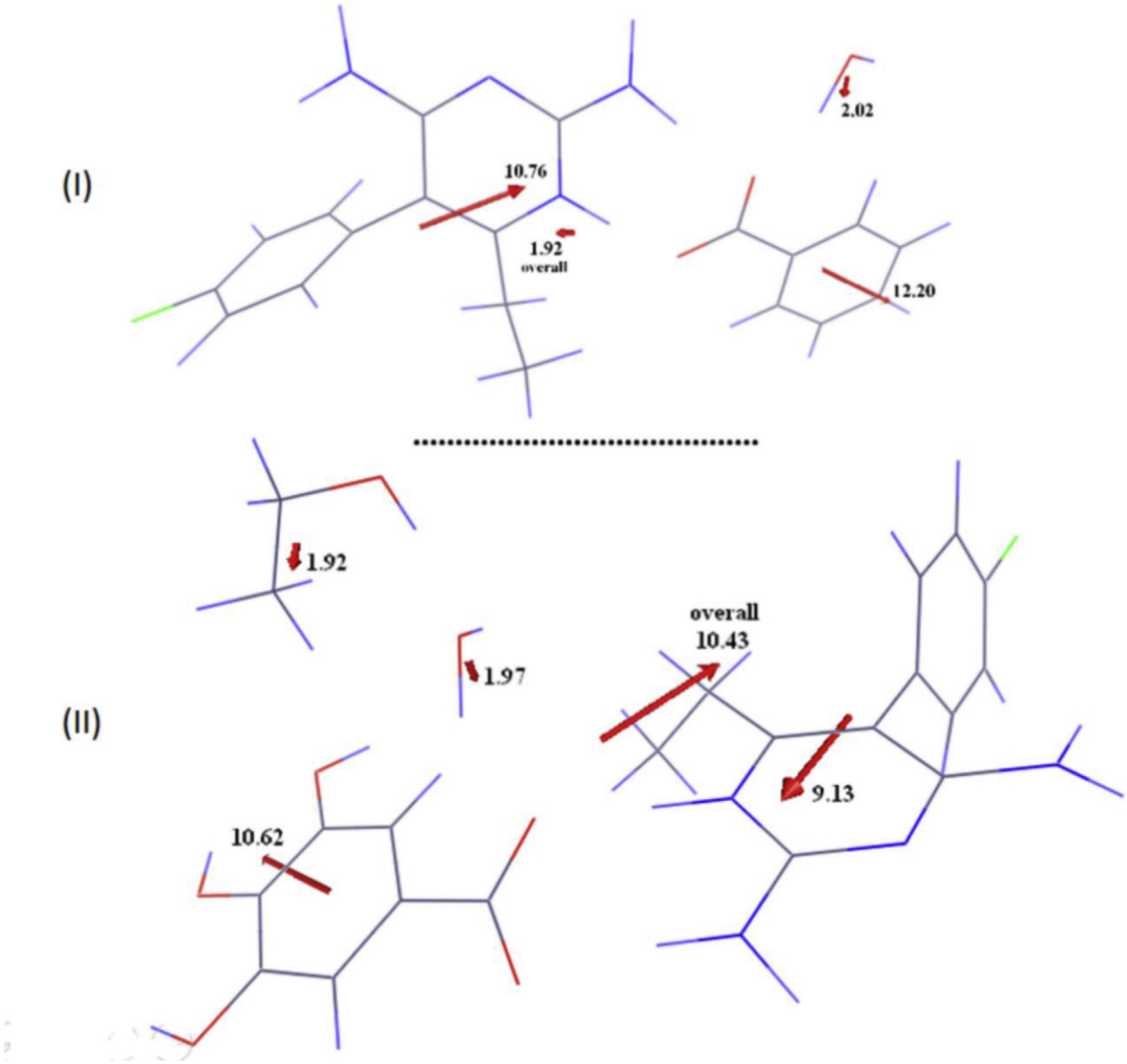

Fig. 6. Showing the dipole moment of both co-crystal moieties. Dipole moment of individual molecule in co-crystal and overall dipole moment of **I** and **II** are illustrated in the diagram.

3.4.2. Compound II

In **II** the electron density is accumulated on all oxygen atoms. Intensity of red color in the ESP diagram shows the negative value of electrostatic potential. The negative electrostatic potential spreads over a wide range of the surface oxygen atoms O1 and O2 in 3, 4, 5-trihydroxybenzoate, O6 in ethanol molecule, O7 in water molecule and N2 in pyrimethaminium cation. Nucleophilic part is also spread by the delocalized electrons of phenolic ring of 3,4,5-trihydroxybenzoate anion. Here also, on one side of the co-crystal moiety in pyrimethaminium cation, from H atoms attached to amine groups to the methyl group, a large region of positive electrostatic potential is displayed but minimum negative charge is also spread along chlorine side of pyrimethamine ring.

Dipole moment of individual moieties of both **I** & **II** co-crystals are shown in Fig (6) and were calculated using MoProviewer [70]. Dipole moment of pyrimethaminium cation in **I** is 10.76D and in **II** is 10.48D. Dipole moment of benzoate anion is 12.20D and 3,4,5-trihydroxybenzoate anion is 10.62D. Dipole moment value of water molecule varies in both co-crystal moieties. In **I** H_2O dipole moment is 1.92D and in **II** it is 1.97D. Ethanol molecule is incorporated in **II**, here its dipole moment is calculated 1.92D. Overall dipole moment of **I** and **II** co-crystal assembly is calculated 1.92D

Table 5
Counterpoise and dispersion corrected Binding Energies (kcal/mol) for the dimeric pairs and trimeric complexes between the constituents, namely; pyrimethamine (A), benzoic acid (B) and water (C) for **I** and pyrimethamine (A), gallic acid (B) and water-ethanol (C) for **II** at M062X-D3/6-31G(d). The values in parenthesis are corresponding BEs (kcal/mol) without Counterpoise corrections.

Type	Compound I	Compound II
$\Delta E_{A\text{-}B}$	−126.3 (−132.7)	−120.1 (−118.4)
$\Delta E_{A\text{-}C}$	−13.04 (−13.99)	−18.15 (−21.67)
$\Delta E_{B\text{-}C}$	−15.75 (−19.38)	−34.16 (−41.14)
$\Delta E_{A\text{-}B\text{-}C}$	−137.1 (−145.8)	−148.8 (−163.3)

Table 6
Bader charges obtained from PBE/PAW periodic DFT-D3 calculations using the QE package. The acronym is adopted from Table 1. The values in parenthesis are corresponding gas phase charges obtained at M062X-D3/6−311++g (2d,2p) using Gaussian 09 package. The charges of individual atoms are given as supporting information.

Constituent	Compound I	Compound II
A	0.788 (0.843)	0.843 (0.864)
B	−0.781 (−0.831)	−0.843 (−0.840)
C	−0.018 (−0.012)	−0.036 (−0.025)

and 10.43D respectively.

3.5. Computational insights

The binding energies (Table 5) of the dimeric pairs and trimeric combination for both **I** and **II** are computed using the relation: $\Delta E_{A\text{-}B} = E_{AB} - E_A - E_B$ and $\Delta E_{A\text{-}B\text{-}C} = E_{ABC} - E_A - E_B - E_C$ respectively. Since ethanol interacts only with water and gallic acid in the asymmetric unit of **II**, we therefore combined both of the solvent molecules during the calculations of binding energies. As expected for **I**, pyrimethamine (A) and benzoic acid (B) form the most stable pair due to the strong N—H···O interactions, and energetically, this pair is the significant contributor in the trimer formation. The water (C) interacts nearly equally with both pyrimethamine and benzoic acid with former interaction being ~2.7 kcal/mol stronger than the later at this level of theory. Similarly, for **II**, the interaction between pyrimethamine (A) and gallic acid (B) is the significant contributor in trimer formation owning to the strong N—H···O bonding, however, this interaction is 6 kcal/mol weaker than the interaction of pyrimethamine with benzoic acid in **I**. Table 5 further reveals, that both water and ethanol in **II**, exhibits higher binding energies with pyrimethamine (A) and gallic acid (B) as compared to the binding of water with similar constituents of **I**. The significant difference can be seen for **II** where the binding between B and C is twofold stronger than the same interaction in **I**. Similarly, the binding between A and C in **II** is ~5 kcal/mol stronger than the same type of interaction in **I**. Though, the binding of pyrimethamine with gallic acid is weaker compared to its interaction with benzoic acid, but the stronger interactions of solvents in **II** imparts higher stabilization to trimer. For both **I** and **II**, the computed binding energies with and without Counterpoise corrections follow the same trend and show significant cooperativity induced stabilization from both hydrogen bonding in co-formers and solvent molecules. Nevertheless, the interaction between A and B in **I** and **II** plays the dominant role in bestowing stability to the trimer.

We performed the Bader charge analysis on the electron density obtained from both periodic and isolated gas phase DFT calculations. The calculated Bader charges of each component of **I** and **II** are listed in Table 6, whereas Table S3 presents the charge on each constituent atom. Though, the charge-based quantum mechanical exploration of intermolecular interactions is a rather complex issue, but in the present study, the charges computed by periodic and gas phase methods are quite consistent, so we may consider them as reliable. The carboxylic carbon C19 of B component is the most electron-depleted atom having charge of 1.65 and 1.60 in **I** and **II** respectively, while the N1 nitrogen atom of pyrimethamine is the electron-richest. The carboxylic group of B components in both cases is considerably polarized, but the negative charge accumulated on both O1 and O2 outweighs the positive charge on C19. In both cases, the same is true for the C8—Cl bonds; however, these are far less polarized. The nitrogen atoms of pyrimethamine in both cases carry nearly equal charge, while, the oxygen of water is slightly more negative in **I** as compared to in **II**. As shown by Table 6, the charge on pyrimethamine (A) is 0.78 and 0.84 in both **I** and **II** respectively, which is considerably less than its formal charge of +1. Similarly, charges on benzoic acid (B) in **I** and gallic acid (B) in

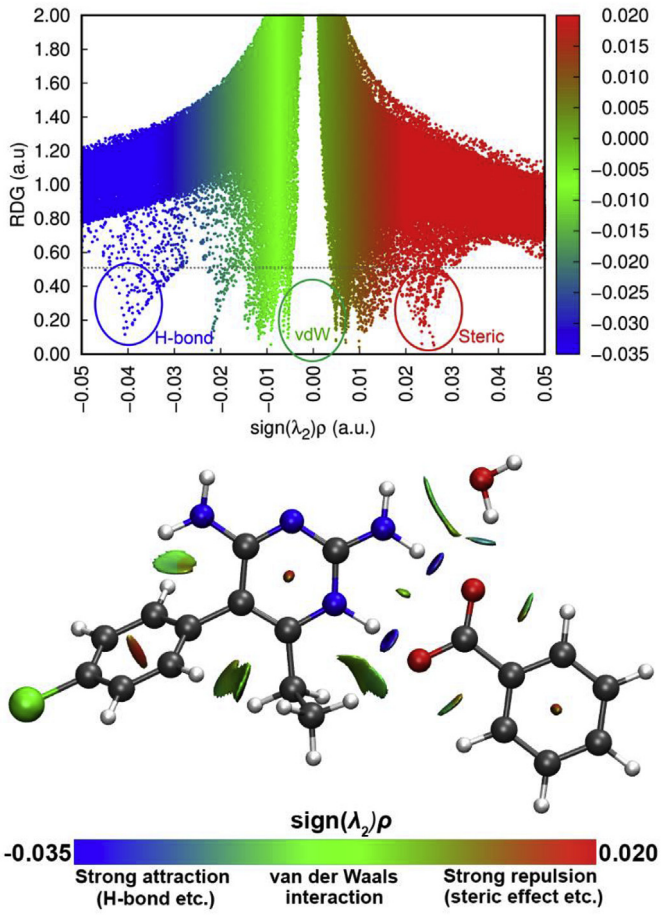

Fig. 7. Plot of RGD vs sign $(\lambda_2)\rho$ for **I**.

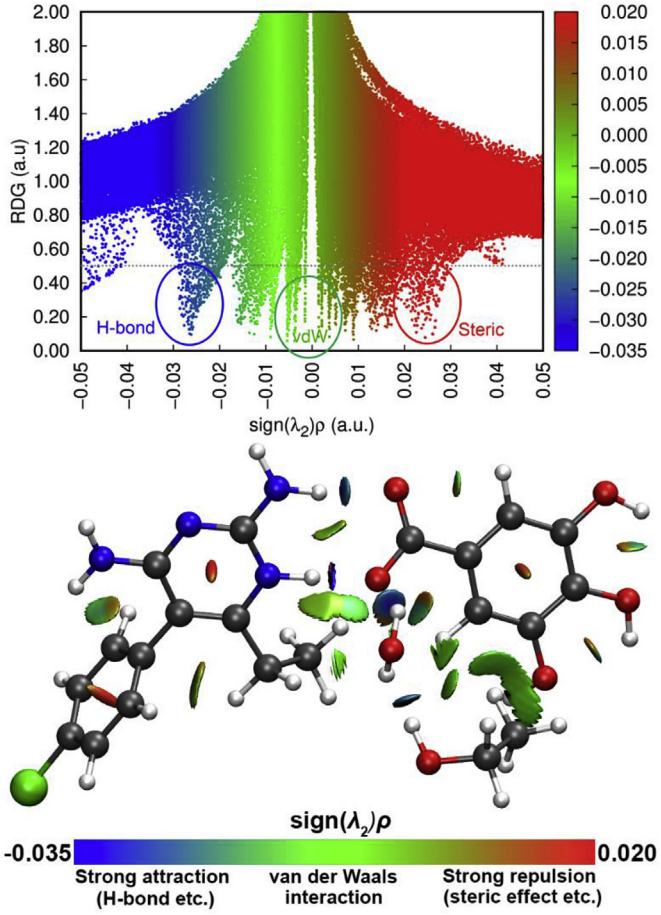

Fig. 8. NCI plot for **II**.

II are −0.78 and −0.84 respectively which are also less than their formal charge of −1. This overestimation of computed charges can be attributed to the very strong N—H···O interaction which restricts the complete proton transfer from benzoic and gallic acid to pyrimethamine. To strengthen this argument, we performed the charge decomposition analysis [94] (CDA) at M062X/6-311 g (2d, 2p) level using the gas phase optimized geometries of dimer AB and fragment A and B of both **I** and **II**. The CDA shows that the net number of electrons transferred from fragment A to B are 0.63 and 0.65 for **I** and **II** respectively which nearly correspond to their charges and small difference can be associated to the contribution of the electron polarization effects. A complementary quantity delocalization index, δ (*1,2*) also termed as Fuzzy bond order [95], measures the number of electrons delocalized or shared between atom 1 and 2 and represents the degree of electron exchange between the basins of 1 and 2. In **I**, δ (O1,H3) is 0.20 which is larger than δ (O2,H1B) (0.10) for a similar type of H-bonded interaction, indicating that former is a much stronger bond and shares more electrons than later. Similarly, the counterpart pair δ (N3, H3) is 0.54 which is smaller than δ (N1, H1B) (0.69) indicating that former shares less electron than the later. The same trend can be seen for **II**, where δ (O2, H3) is 0.15 larger than δ (O1, H1A) that is 0.07 and δ (N3, H3) is 0.60 smaller than δ (N1, H1A) that is 0.72. These results of delocalization indices strengthen the argument that the overestimation of charges is associated with incomplete proton transfer between component B and component A in both cases. This argument can be further complimented from the lengthening of N3—H3 bond (1.06 Å) in pyrimethamine as compared to other N—H (1.03 Å) bonds of the pyrimethamine moiety which are involved in similar types of H-bonding interactions.

The noncovalent interaction (NCI) [96] method also known as reduced density gradient (RDG) method provides a robust methodology to visualize the weak interactions including the van der Waals (vdW) and dispersion interactions.

The top of Fig. 7 presents the plot of RGD versus the $sign(\lambda_2)\rho$ plot for **I** and bottom shows the various types of interactions in the real space of the molecule. The majority of interactions between different constituents of **I** mainly consists of vdW types of interactions as revealed by the dominant green color in the bottom figure and spikes located around zero on top figure. The only stronger attractive interaction *i.e.* the hydrogen bonding is present between the pyrimethamine and the carboxylic group of benzoic acid. The interactions between water and both of the other components are much weaker than the aforementioned interactions. This indicates that though water is important for unit cell packing but the significant role for dimer formation is only played by the hydrogen bonding interaction between the major components of **I**.

Fig. 8 shows NCI plots for **II** and presents similar findings. However, in contrast to **I**, the water molecule is involved in a strong H-bonding interaction with the carboxylic oxygen of gallic acid and compliments their binding energies mentioned in Table 5. The relative comparison of NCI plot and binding energies for both systems suggest that higher binding energy of **II** is due to the stability imparted by the H-bonding of solvent molecules. From the analyses performed until now, it is clear that the presence of a variety of intermolecular forces between the constituent molecules leads to the co-crystal formation.

3.6. TGA analysis

3.6.1. Compound I

The thermal analysis was performed on a PerkinElmer STA 6000 simultaneous TGA/DSC instrument. It is done to investigate thermal stability of material. 2 mg sample was added to crucible and it was heated from 30 °C to 500 °C at a rate of 20 °C/min under continuous purging of nitrogen gas. With increase in temperature, the decomposition of mass is indicated by endothermic peak in TGA plot. The TGA/DSC data curve shows the thermal behavior of Pyrimethamine, benzoic acid and water cocrystal. The combustion of material occurs in temperature range between 120 °C to 300 °C. The melting point of Pyrimethamine is 233 °C and melting point of co-former benzoic acid is 122 °C.The TGA data shows that up to

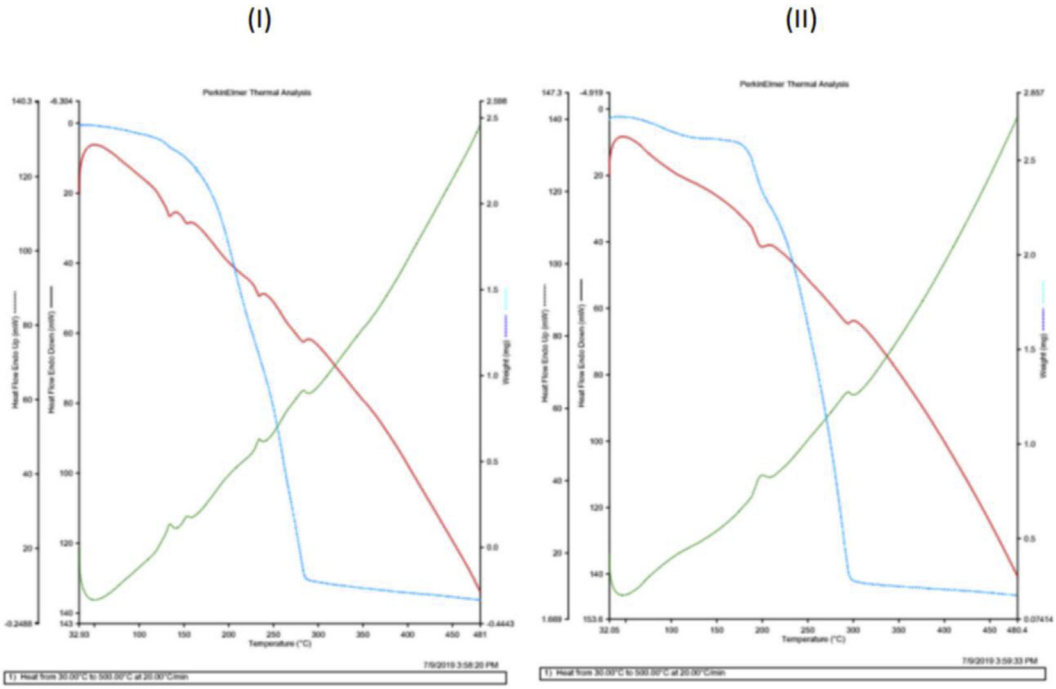

Fig. 9. Thermogravimetric analysis plot.

temperature 120 °C, there is no loss of any component and the structure is stable at that temperature. A sharp endothermic peak is obtained at 122 °C a temperature which is actually the melting point of benzoic acid. The endothermic peaks are not sharp, which indicates that crystallinity of sample is not good. After 122 °C, the decomposition of material starts. The second endothermic peak is observed at 300 °C which confirms further decomposition of sample. After 300 °C, the sample disintegrates completely.

3.6.2. Compound II

The TGA-DSC data curve shows the thermal behavior of Pyrimethamine, Gallic acid and water co-crystal. The decomposition of mass occurs in temperature range between 230 °C to 300 °C. The melting point of Pyrimethamine is 233 °C and melting point of co-former Gallic acid is 260 °C. The TGA data shows that up to temperature 233 °C, there is no loss of any component and the structure is stable at that temperature. A sharp endothermic peak is obtained

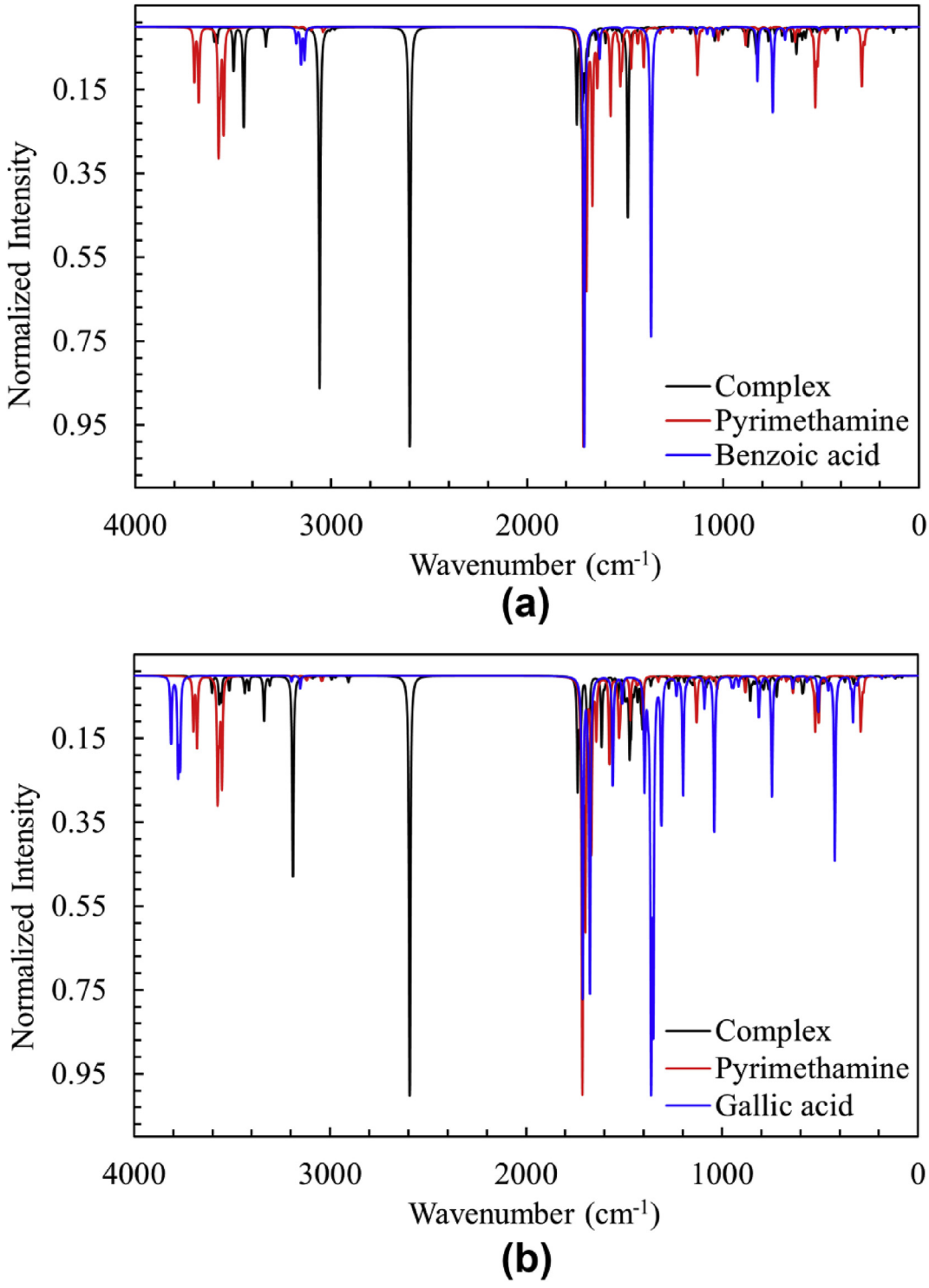

Fig. 10. Calculated IR spectra of (a) **I** and (b) **II** and their individual components.

at a temperature which is actually the melting point of molecule. The endothermic peaks are not sharp, which indicates that crystallinity of sample is not good. After 233 °C the decomposition of sample starts. The second endothermic peak is observed at 290 °C which confirms further decomposition of sample. After 300 °C, the sample evaporates completely. TGA plots of both molecules **I** and **II** are shown in Fig. 9.

3.7. Simulated IR spectra

Fig. 10 presents the normalized IR intensities of both **I** and **II** and their individual components simulated at M06−2X/6−311 + g (2d, 2p) level of DFT calculations. The IR spectra of pyrimethamine (red) shows two small peaks at 292 and 529 cm^{-1} which mainly corresponds to the out of plane twisting vibrations of $-NH_2$ and −NH respectively. A small peak at 1130 cm^{-1} can be assigned to the stretching vibrations of C−Cl bond. The major peak positioned at 1712 cm^{-1} is associated to the C = N stretching vibrations combined with in-plane scissoring mode of $-NH_2$ hydrogens. Two splits peaks at 3550 and 3680 cm^{-1} represents the symmetric and asymmetric stretching vibrations of N−H hydrogens. Fig. 10(a) exhibits that the out of plane wagging vibrations of C−H bonds in benzoic acid (blue) can be linked with a small peak at 746 cm^{-1} whereas a neighboring peak position at 824 cm^{-1} is associated with the stretching vibrations of C = C bonds of phenyl and carboxylic carbon atoms. A medium-to-large peak at 1367 cm^{-1} and a large peak at 1709 cm^{-1} represents the symmetric and asymmetric stretching vibrations respectively in C = O bond of carboxylic group. The IR intensity spectra of **I** (black line) in Fig. 10(a) shows that a peak positioned at 1486 cm^{-1} is associated with the stretching vibration of C = O bond of carboxylic group of benzoic acid combined with C = N stretching vibrations of pyrimethamine. However, the signature intensity peaks for **I** are positioned at 2600 and 3060 cm^{-1} which represent the symmetric stretching vibrations of N−H···O hydrogen bonds between pyrimethamine and benzoic acid where the former corresponds to vibrations of transferred proton between both components whereas the latter is associated with hydrogen bonded $-NH_2$ group. In addition to these peaks, a small peak at 3450 cm^{-1} represents the O−H···O interaction between benzoic acid and water molecule.

Similarly, as shown in Fig. 10(b) the hydroxyl hydrogens in gallic acid (blue) show a wagging vibrational mode at 424 cm^{-1}. Two medium peaks at 750 and 1040 cm^{-1} can be associated to the stretching of C = C bonds in phenyl ring and hydroxyl C−O bonds respectively. The major intensity peak at 1360 cm^{-1} represents the stretching vibrations of C−C bond of phenyl and carboxylic carbon atoms. Similarly, two neighboring peaks at 1670 and 1710 cm^{-1} shows the symmetric stretching and of C = C bonds and asymmetric stretching of C = O bond of carboxylic group. A small peak at 3760 cm^{-1} indicates the stretching vibration of O−H bond in hydroxyl group. Since complex **I** and **II** involve similar type of hydrogen bonded interactions, therefore their IR intensity peaks are positioned at nearly same frequencies. Like **I**, the two signature peaks of **II** (black) are located at 2600 and 3200 cm^{-1} representing the stretching of involved hydrogen bonds.

4. Conclusion and perspective

Using a synthon-based approach, we have successfully synthesized co-crystal of pyrimethamine with benzoic acid and 3,4,5-trihydroxybenzoic acid. The co-crystal structure was refined using spherical atomic model (IAM) and multipolar atomic model by transferring electron density parameters from ELMAM2. In I and II we used DFT distances calculated theoretically instead of neutron distances. We observed that distances calculated from DFT shows a good improvement in statistical indexes as compared with neutron distances in both compounds. Furthermore, library transfer in both I and II cases, owing to an improved model, results in better figure of merits such that lower crystallographic R factor, weighted R factor and better goodness of fit. The calculated stabilization energies, charge transfer and non-covalent interactions (NCI) analysis indicate a significant contribution of hydrogen bonding between co-formers vis-à-vis solvent molecules to stabilize the molecules in co-crystals of both **I** and **II**. The structure of co-crystal assembly is stabilized by strong electrostatic attraction between charged ionic species due to shifting of proton from co-formers to pyrimethamine (benzoic acid to pyrimethamine and from 3,4,5-trihydroxybenzoic acid to pyrimethamine). Transferability principle helps for better analysis of crystal structure and results in improved model and better refinement statistics for ordinary data collected at room temperature.

Author contribution

Maqsood Ahmed and Sajida Noureen originally devised the project and procured the materials. Muhammad Umer Faroque prepared the samples and the initial draft of the manuscript. Maqsood Ahmed collected the diffraction, solved and refined the structure. Sajida Noureen carried out thermal analysis. Arshad Mehmood carried out theoretical calculations and wrote down the theoretical section. All the authors reviewed the manuscript.

Declaration of competing interest

The authors declare no competing interests.

Acknowledgement

The authors acknowledge funding from the Higher Education Commission (HEC) of Pakistan for the establishment of Materials Chemistry Laboratory.

Appendix A. Supplementary data

Supplementary data to this article can be found online at https://doi.org/10.1016/j.molstruc.2020.128183.

References

[1] W. Zhu, et al., Challenges of organic “cocrystals”, Science China Materials 58 (11) (2015) 854−859.
[2] Z. Weigang, et al., Organic Cocrystal Optoelectronic Materials and Devices, 2014.
[3] J.T. Jones, et al., Modular and predictable assembly of porous organic molecular crystals, Nature 474 (7351) (2011) 367−371.
[4] H.G. Brittain, Cocrystal systems of pharmaceutical interest: 2010, Cryst. Growth Des. 12 (2) (2012) 1046−1054.
[5] Ö. Almarsson, M.J. Zaworotko, Crystal engineering of the composition of pharmaceutical phases. Do pharmaceutical co-crystals represent a new path to improved medicines? Chem. Commun. (17) (2004) 1889−1896.
[6] G. Bolla, A. Nangia, Pharmaceutical cocrystals: walking the talk, Chem. Commun. 52 (54) (2016) 8342−8360.
[7] S. Aitipamula, P.S. Chow, R.B.H. Tan, Trimorphs of a pharmaceutical cocrystal involving two active pharmaceutical ingredients: potential relevance to combination drugs, CrystEngComm 11 (9) (2009) 1823−1827.
[8] P. Vishweshwar, et al., Pharmaceutical co-crystals, J. Pharmaceut. Sci. 95 (3) (2006) 499−516.
[9] O.N. Kavanagh, et al., Pharmaceutical cocrystals: from serendipity to design to application, Drug Discov. Today 24 (3) (2019) 796−804.
[10] G.R. Desiraju, Hydrogen bridges in crystal Engineering: interactions without borders, Acc. Chem. Res. 35 (7) (2002) 565−573.
[11] C.A. Lipinski, et al., Experimental and computational approaches to estimate solubility and permeability in drug discovery and development settings, Adv. Drug Deliv. Rev. 46 (1−3) (2001) 3−26.
[12] T. Wang, et al., Salts, cocrystals, and ionic cocrystals of a “simple” tautomeric compound, Cryst. Growth Des. 18 (11) (2018) 6973−6983.

[13] G.R. Desiraju, Chemistry beyond the molecule, Nature 412 (6845) (2001) 397.
[14] L.J. Prins, D.N. Reinhoudt, P. Timmerman, Noncovalent synthesis using hydrogen bonding, Angew. Chem. Int. Ed. 40 (13) (2001) 2382–2426.
[15] L.-L. Han, et al., Solution and mechanochemical syntheses of two novel cocrystals: ligand length modulated interpenetration of hydrogen-bonded 2D 63-hcb networks based on a robust trimeric heterosynthon, Cryst. Growth Des. 14 (3) (2014) 1221–1226.
[16] C.B. Aakeröy, Crystal engineering: strategies and architectures, Acta Crystallogr. Sect. B Struct. Sci. 53 (4) (1997) 569–586.
[17] D. Sun, et al., Solvent-Controlled rare case of a triple helical molecular braid assembled from proton-transferred sebacic acid, Cryst. Growth Des. 11 (8) (2011) 3323–3327.
[18] D. Sun, et al., A novel silver(I)-containing supramolecular framework incorporating eight different hydrogen bond motifs, J. Mol. Struct. 969 (1) (2010) 176–181.
[19] E.S. Hurwitz, Reye's syndrome, Epidemiol. Rev. 11 (1989) 249–253.
[20] K.G. Lewis, R.G. Dufresne Jr., A meta-analysis of complications attributed to anticoagulation among patients following cutaneous surgery, Dermatol. Surg. 34 (2) (2008) 160–165.
[21] C.P. Brock, J.D. Dunitz, F.L. Hirshfeld, Transferability of deformation densities among related molecules: atomic multipole parameters from perylene for improved estimation of molecular vibrations in naphthalene and anthracene, Acta Crystallogr. B 47 (5) (1991) 789–797.
[22] C.P. Brock, J. Dunitz, F. Hirshfeld, Transferability of deformation densities among related molecules: atomic multipole parameters from perylene for improved estimation of molecular vibrations in naphthalene and anthracene, Acta Crystallogr. Sect. B Struct. Sci. 47 (5) (1991) 789–797.
[23] P.M. Dominiak, et al., A theoretical databank of transferable aspherical atoms and its application to electrostatic interaction energy calculations of macromolecules, J. Chem. Theor. Comput. 3 (1) (2007) 232–247.
[24] B. Dittrich, et al., Introduction and validation of an invariom database for amino-acid, peptide and protein molecules, Acta Crystallogr. Sect. D Biol. Crystallogr. 62 (11) (2006) 1325–1335.
[25] B. Zarychta, et al., On the application of an experimental multipolar pseudo-atom library for accurate refinement of small-molecule and protein crystal structures, Acta Crystallogr. A: Foundations of Crystallography 63 (2) (2007) 108–125.
[26] S. Domagała, et al., An improved experimental databank of transferable multipolar atom models–ELMAM2. Construction details and applications, Acta Crystallogr. A: Foundations of Crystallography 68 (3) (2012) 337–351.
[27] B. Dittrich, et al., The invariom model and its application: refinement of D, L-serine at different temperatures and resolution, Acta Crystallogr. A: Foundations of Crystallography 61 (3) (2005) 314–320.
[28] B. Dittrich, P. Munshi, M. Spackman, Redetermination, invariom-model and multipole refinement of l-ornithine hydrochloride, Acta Crystallogr. Sect. B Struct. Sci. 63 (3) (2007) 505–509.
[29] B. Dittrich, J. McKinnon, J. Warren, Improvement of anisotropic displacement parameters from invariom-model refinements for three L-hydroxylysine structures, Acta Crystallogr. Sect. B Struct. Sci. 64 (6) (2008) 750–759.
[30] B. Dittrich, et al., Towards extracting the charge density from normal-resolution data, J. Appl. Crystallogr. 42 (6) (2009) 1110–1121.
[31] B. Dittrich, et al., Invariоms for improved absolute structure determination of light-atom crystal structures, Acta Crystallogr. A: Foundations of Crystallography 62 (3) (2006) 217–223.
[32] M.L. Gatton, L.B. Martin, Q. Cheng, Evolution of Resistance to Sulfadoxine-Pyrimethamine in Plasmodium falciparum</em&gt, Antimicrob. Agents Chemother. 48 (2004) 2116, 0.
[33] C. Sirichaiwat, et al., Target guided synthesis of 5-Benzyl-2,4-diamonopyrimidines: their antimalarial activities and binding affinities to wild type and mutant dihydrofolate reductases from plasmodium falciparum, J. Med. Chem. 47 (2) (2004) 345–354.
[34] G. Indrayanto, et al., Benzoic acid, in: H.G. Brittain (Ed.), Analytical Profiles of Drug Substances and Excipients, Academic Press, 1999, pp. 1–46.
[35] A. Chanwitheesuk, et al., Antimicrobial gallic acid from Caesalpinia mimosoides Lamk, Food Chem. 100 (3) (2007) 1044–1048.
[36] A.K. Pandurangan, et al., Gallic acid attenuates dextran sulfate sodium-induced experimental colitis in BALB/c mice, Drug Des. Dev. Ther. 9 (2015) 3923–3934.
[37] K. Koyama, N. Goto-Yamamoto, K. Hashizume, Influence of maceration Temperature in red wine Vinification on Extraction of Phenolics from berry Skins and Seeds of grape (Vitis vinifera), Biosc. Biotech. Biochem. 71 (4) (2007) 958–965.
[38] S. Choubey, et al., Medicinal importance of gallic acid and its ester derivatives: a patent review, Pharmaceutical Patent Analyst 4 (4) (2015) 305–315.
[39] R.-F. Liao, J.W. Lauher, F.W. Fowler, The application of the 2-amino-4-pyrimidones to supramolecular synthesis, Tetrahedron 52 (9) (1996) 3153–3162.
[40] Y.-J. Li, et al., The length of ankyl chain tuning the structure and properties of organic assemblies composed of triazole and organic acids, J. Mol. Struct. 1153 (2018) 96–105.
[41] N.N. Adarsh, D.K. Kumar, P. Dastidar, Composites of N,N′-bis-(pyridyl) urea-dicarboxylic acid as new hydrogelators—a crystal engineering approach, Tetrahedron 63 (31) (2007) 7386–7396.
[42] X. Fu, et al., A new family of insensitive energetic copolymers composed of nitro and nitrogen-rich energy components: structure, physicochemical property and density functional theory, J. Anal. Appl. Pyrol. 114 (2015) 79–90.
[43] C. Balakrishnan, et al., Synthesis, crystal growth, structural characterization and theoretical investigations of bis (benzene-1, 2-dicarboxylato) bis (thiourea) zinc, Mol. Cryst. Liq. Cryst. 664 (1) (2018) 182–194.
[44] J.-W. Zhao, et al., Novel one-dimensional organic–inorganic polyoxometalate hybrids constructed from heteropolymolybdate units and copper–aminoacid complexes, Cryst. Growth Des. 14 (3) (2014) 1467–1475.
[45] L.S. Reddy, et al., Hydrogen bonding in crystal structures of N, N '-Bis (3-pyridyl) urea. Why is the N– H⊙⊙⊙ O tape synthon absent in diaryl ureas with electron-withdrawing groups? Cryst. Growth Des. 6 (1) (2006) 161–173.
[46] J. Han, et al., Anionic host layers constructed with guanidinium–hydrogen carbonate dimer 2: 1 rosette-ribbons and bridging carboxylate connectors, Cryst. Growth Des. 12 (9) (2012) 4457–4465.
[47] M.B. Cingi, et al., The crystal and molecular structure of tris (thiourea) copper (I) hydrogen-o-phthalate. A monomeric trigonal planar copper (I) complex, Acta Crystallogr. B Struct. Crystallogr. Cryst. Chem. 33 (12) (1977) 3772–3777.
[48] I. Matulková, I. Císařová, I. Němec, 2-Phenylbiguanidinium hydrogen succinate methanol monosolvate, Acta Crystallogr. E: Structure Reports Online 66 (12) (2010) o3187–o3188.
[49] R.-B. Zhang, et al., Synthesis, structure, and physical properties of a new anions-controlled Cd (II)-guanazole (3, 5-diamino-1, 2, 4-triazole) hybrid family, Inorg. Chem. 47 (11) (2008) 4861–4876.
[50] X. Liu, et al., Structure, physicochemical properties, and density functional theory calculation of high-energy-density materials constructed with intermolecular interaction: nitro group charge determines sensitivity, J. Phys. Chem. C 118 (41) (2014) 23487–23498.
[51] D. Kalita, J.B. Baruah, 1-Phenyl-3-(quinolin-5-yl) urea as a host for distinction of phthalic acid and terephthalic acid, J. Chem. Sci. 125 (2) (2013) 267–273.
[52] I. Leban, A. Rupnik, Structure of guanidinium hydrogen acetylenedicarboxylate, CH6N3+. C4HO4–, Acta Crystallogr. Sect. C Cryst. Struct. Commun. 48 (5) (1992) 821–824.
[53] Q. Li, T.C. Mak, Inclusion compounds of thiourea and peralkylated ammonium salts. Part V. Hydrogen-bonded host lattices built of thiourea and acetate ions, J. Inclusion Phenom. Mol. Recognit. Chem. 28 (3) (1997) 183–204.
[54] S.-L. Li, et al., trans-Diaquabis (thiosemicarbazido-κ2N, S) nickel (II) dimaleate dihydrate, Acta Crystallogr. Sect. C Cryst. Struct. Commun. 59 (5) (2003) m181–m183.
[55] S.-L. Li, et al., Bis (thiosemicarbazide) zinc (II) bis (maleate) dihydrate, Acta Crystallogr. E: Structure Reports Online 61 (12) (2005) m2701–m2703.
[56] S.L. Li, et al., Bis (thiosemicarbazide) zinc (II) bis (maleate) dihydrate, *Erratum.* Acta Crystallographica Section E 62 (1) (2006) e1-e1.
[57] S. Murugavel, et al., Aminoguanidinium hydrogen fumarate, Acta Crystallogr. E: Structure Reports Online 65 (3) (2009) o548-o548.
[58] Y. Yan, J.-M. Chen, T.-B. Lu, Simultaneously enhancing the solubility and permeability of acyclovir by crystal engineering approach, CrystEngComm 15 (33) (2013) 6457–6460.
[59] Y. Yokomori, D.J. Hodgson, Guanidinium-carboxylate interactions: II. Crystal structures of methylguanidinium benzylhydrogenmalonate, methylguanidinium ethylhydrogenmalonate, and methylguanidinium sulfate, Int. J. Pept. Protein Res. 31 (3) (1988) 289–298.
[60] F. Dai, et al., Conformation variation of tris(2-carboxyethyl)isocyanuric acid induced by cocrystallized N-heterocyclic organic molecules, CrystEngComm 14 (4) (2012) 1376–1381.
[61] O.V. Dolomanov, et al., OLEX2: a complete structure solution, refinement and analysis program, J. Appl. Crystallogr. 42 (2) (2009) 339–341.
[62] G.M. Sheldrick, Acta Cryst. C71 (2015) 3–8.
[63] L.J. Farrugia, WinGX and ORTEP for Windows: an update, J. Appl. Crystallogr. 45 (4) (2012) 849–854.
[64] C.F. Macrae, et al., Mercury CSD 2.0—new features for the visualization and investigation of crystal structures, J. Appl. Crystallogr. 41 (2) (2008) 466–470.
[65] C. Jelsch, et al., Advances in protein and small-molecule charge-density refinement methods using MoPro, J. Appl. Crystallogr. 38 (1) (2005) 38–54.
[66] F.H. Allen, I.J. Bruno, Bond lengths in organic and metal-organic compounds revisited: X—H bond lengths from neutron diffraction data, Acta Crystallogr. Sect. B Struct. Sci. 66 (3) (2010) 380–386.
[67] A.Ø. Madsen, SHADE web server for estimation of hydrogen anisotropic displacement parameters, J. Appl. Crystallogr. 39 (5) (2006) 757–758.
[68] M.U. Faroque, et al., Electrostatic properties of the pyrimethamine–2, 4-dihydroxybenzoic acid cocrystal in methanol studied using transferred electron-density parameters, Acta Crystallogr. C: Struct. Chem. 74 (1) (2018) 100–107.
[69] R. Herbst-Irmer, et al., Anharmonic motion in experimental charge density investigations, J. Phys. Chem. 117 (3) (2013) 633–641.
[70] S. Domagała, et al., Structural analysis and multipole modelling of quercetin monohydrate—a quantitative and comparative study, Acta Crystallogr. Sect. B Struct. Sci. 67 (1) (2011) 63–78.
[71] V. Pichon-Pesme, et al., A comparison between experimental and theoretical aspherical-atom scattering factors for charge-density refinement of large molecules, Acta Crystallogr. A: Foundations of Crystallography 60 (3) (2004) 204–208.
[72] P. Giannozzi, et al., Advanced capabilities for materials modelling with Quantum ESPRESSO, J. Phys. Condens. Matter 29 (46) (2017) 465901.
[73] J.P. Perdew, K. Burke, M. Ernzerhof, Generalized gradient approximation made simple, Phys. Rev. Lett. 77 (18) (1996) 3865–3868.

[74] S. Grimme, et al., A consistent and accurate ab initio parametrization of density functional dispersion correction (DFT-D) for the 94 elements H-Pu, J. Chem. Phys. 132 (15) (2010) 154104.
[75] P.E. Blöchl, Projector augmented-wave method, Phys. Rev. B 50 (24) (1994) 17953–17979.
[76] W. Tang, E. Sanville, G. Henkelman, A grid-based Bader analysis algorithm without lattice bias, J. Phys. Condens. Matter 21 (8) (2009), 084204.
[77] Frisch, M.J., et al., *Gaussian 09*. 2009, Gaussian, Inc.: Wallingford, CT, USA.
[78] Y. Zhao, D.G. Truhlar, The M06 suite of density functionals for main group thermochemistry, thermochemical kinetics, noncovalent interactions, excited states, and transition elements: two new functionals and systematic testing of four M06-class functionals and 12 other functionals, Theoretical Chemistry Accounts 120 (1) (2008) 215–241.
[79] S.F. Boys, F. Bernardi, The calculation of small molecular interactions by the differences of separate total energies. Some procedures with reduced errors, Mol. Phys. 19 (4) (1970) 553–566.
[80] T. Lu, F. Chen, Multiwfn: a multifunctional wavefunction analyzer, J. Comput. Chem. 33 (5) (2012) 580–592.
[81] D. Hirshfeld, Y. Radzyner, D. Rapaport, Molecular dynamics studies of granular flow through an aperture, Phys. Rev. 56 (4) (1997) 4404.
[82] J.J. McKinnon, M.A. Spackman, A.S. Mitchell, Novel tools for visualizing and exploring intermolecular interactions in molecular crystals, Acta Crystallogr. Sect. B Struct. Sci. 60 (6) (2004) 627–668.
[83] R. Bader, T. Nguyen-Dang, Quantum theory of atoms in molecules–Dalton revisited, in: Advances in Quantum Chemistry, Elsevier, 1981, pp. 63–124.
[84] E. Mupere, et al., Measles vaccination effectiveness among children under 5 years of age in Kampala, Uganda, Vaccine 24 (19) (2006) 4111–4115.
[85] D. Cremer, E. Kraka, Chemical bonds without bonding electron density—does the difference electron-density analysis suffice for a description of the chemical bond? Angew Chem. Int. Ed. Engl. 23 (8) (1984) 627–628.
[86] D.S. Arputharaj, et al., Topological electron density analysis and electrostatic properties of aspirin: an experimental and theoretical study, Cryst. Growth Des. 12 (9) (2012) 4357–4366.
[87] E.A. Zhurova, et al., Experimental and theoretical electron density study of estrone, J. Am. Chem. Soc. 128 (27) (2006) 8849–8861.
[88] E.A. Zhurova, et al., Charge density and electrostatic potential study of 16α, 17β-estriol and the binding of estrogen molecules to the estrogen receptors ERα and ERβ, J. Phys. Chem. B 120 (34) (2016) 8882–8891.
[89] E.J. Yearley, et al., Binding of genistein to the estrogen receptor based on an experimental electron density study, J. Am. Chem. Soc. 129 (48) (2007) 15013–15021.
[90] C. Kalaiarasi, M.S. Pavan, P. Kumaradhas, Topological characterization of electron density, electrostatic potential and intermolecular interactions of 2-nitroimidazole: an experimental and theoretical study, Acta Crystallogr. B: Structural Science, Crystal Engineering and Materials 72 (5) (2016) 775–786.
[91] P. Kumar, P.M. Dominiak, Structural and dynamical aspects of electrostatic interactions by applying aspherical atom model in HIV-1 protease, Biophys. J. 110 (3) (2016) 380a.
[92] G. Rajalakshmi, V.R. Hathwar, P. Kumaradhas, Intermolecular interactions, charge-density distribution and the electrostatic properties of pyrazinamide anti-TB drug molecule: an experimental and theoretical charge-density study, Acta Crystallogr. B: Structural Science, Crystal Engineering and Materials 70 (3) (2014) 568–579.
[93] B. Fournier, et al., Charge density and electrostatic interactions of fidarestat, an inhibitor of human aldose reductase, J. Am. Chem. Soc. 131 (31) (2009) 10929–10941.
[94] S. Dapprich, G. Frenking, Investigation of donor-acceptor interactions: a charge decomposition analysis using fragment molecular orbitals, J. Phys. Chem. 99 (23) (1995) 9352–9362.
[95] I. Mayer, P. Salvador, Overlap populations, bond orders and valences for 'fuzzy' atoms, Chem. Phys. Lett. 383 (3) (2004) 368–375.
[96] E.R. Johnson, et al., Revealing noncovalent interactions, J. Am. Chem. Soc. 132 (18) (2010) 6498–6506.